

Core-Shell Structured CoP@C Cubes as a Superior Anode for High-Rate and Stable Sodium Storage

Lingbo Ren,^[a, b] Yueying Li,^{*[a]} Zhidong Hou,^[b] and Jian-Gan Wang^{*[a, b]}

Transition metal phosphides have emerged as a class of promising anode materials of sodium-ion batteries owing to their excellent sodium storage capacity. However, the limited electronic conductivity and significant volume expansion have impeded their further advancement. In this work, we propose a rational design of cube-like CoP @C composites with unique core-shell structure *via* *in situ* phosphating and subsequent carbon coating processes. The uniform carbon coating serves as a physical buffering layer that effectively mitigates volume changes during charge/discharge processes, and prevents

particle agglomeration and fragmentation, thereby enhancing the structural stability of electrode. Moreover, the nitrogen-rich carbon layer not only provides additional active sites for sodium ion adsorption but also improves the electrode conductivity and accelerates charge transport dynamics. Consequently, the as-synthesized CoP@C exhibits a remarkable capacity retention rate of 94.8% after 100 cycles at 0.1 A g^{-1} and achieves a high reversible capacity of 146.7 mAh g^{-1} even under a high current density of 4.0 A g^{-1} .

1. Introduction

Sodium-ion batteries (SIBs) are regarded as a promising energy storage technology in the post-lithium-ion battery era due to their abundant sodium resources and attractive cost-effectiveness.^[1] However, the larger ionic radius (1.02 \AA)^[2] and heavier relative atomic mass (23 g mol^{-1})^[3] of sodium ions result in sluggish redox kinetics, inevitably leading to significant structural distortion during insertion/removal processes,^[4] which hampers the electrochemical performance of SIBs. Therefore, there is an urgent demand for developing high-performance anodes tailored for SIBs to enhance charge transfer dynamics and alleviate volume changes during repetitive cycles.

Transition metal phosphates (TMPs) have garnered significant attention as a promising class of conversion-type anode materials for SIBs, in virtue of their high theoretical specific capacity and suitable sodiation potential.^[5] However, TMPs still face challenges such as poor inherent electronic conductivity and severe volume expansion, resulting in subpar rate performance and limited cycle life.^[6] To address these issues, several modification strategies have been proposed,^[7] including the design of unique micro/nanostructures^[8] and composites with conductive matrices^[9] to facilitate electron transfer, buffer volume changes, and enhance electrode structure stability.

Recently, Prussian blue analogs (PBAs) have emerged as efficient template precursors for synthesizing metal compounds with diverse topologies and compositions.^[10] The distinctive open frame structure of PBAs imparts derived metal compounds with advantages such as high specific surface area and large pore volume^[11] that not only promote rapid electrolyte penetration but also effectively mitigate volume changes during sodiation/desodiation processes. Furthermore, carbon-coated core-shell electrodes could further improve electrochemical performance by enhancing the conductivity of hybrid electrodes while preventing crushing and aggregation of internal active substances during repeated charge/discharge cycles, enabling fast reaction kinetics and long cycle lifespan.^[12]

In this study, we report a rational synthesis of carbon-coated CoP (CoP@C) core-shell cubes by employing a facile phosphating and subsequent carbonization method. When utilized as the anode of SIBs, the carbon coating layer effectively mitigates volume changes during repeated charge/discharge processes, prevents particle aggregation and crushing, and thus enhances structural stability accordingly. Moreover, the nitrogen-doped carbon further improves the electrical conductivity, which facilitates rapid electron/ion transport and enhanced electrochemical reaction kinetics. Benefiting from these favorable merits, the CoP@C electrode exhibits excellent capacity retention with a high rate of 94.8% after 100 cycles at 0.1 A g^{-1} , while maintaining a remarkable reversible capacity of 146.7 mAh g^{-1} even at a high current density of 4.0 A g^{-1} .

2. Results and Discussion

The synthesis process of core-shell structured CoP@C cube composites is illustrated in Figure 1. Initially, CoCo-PBA cubes are prepared as the precursor using a facile coprecipitation method.^[13] Subsequently, NaH_2PO_2 is utilized as the phosphorus source for low-temperature phosphating. During this pro-

[a] L. Ren, Y. Li, J.-G. Wang
School of Energy and Electrical Engineering, Qinghai University,
Xi'an 810016, China
E-mail: liyy2019@qhu.edu.cn

[b] L. Ren, Z. Hou, J.-G. Wang
State Key Laboratory of Solidification Processing, Center for Nano Energy Materials, School of Materials Science and Engineering, Northwestern Polytechnical University and Shaanxi Joint Lab of Graphene (NPU), No. 127, Youyi West Road, Xi'an 710072, China
E-mail: wangjiangan@nwpu.edu.cn

 Supporting information for this article is available on the WWW under <https://doi.org/10.1002/batt.202400471>

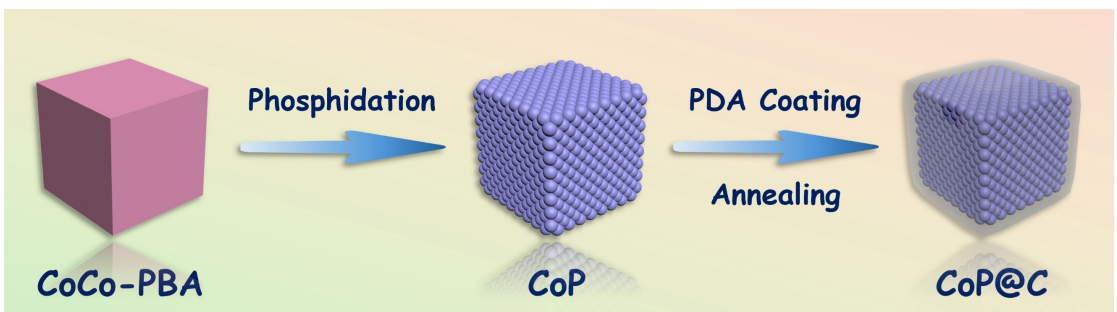


Figure 1. The synthesis process diagram of core-shell structured CoP@C cubes.

ture, CoCo-PBA reacts with PH_3 gas generated from the thermal decomposition of NaH_2PO_2 to form three-dimensional porous CoP intermediates. After annealing in an inert atmosphere, the uniformed polydopamine (PDA) layer is converted to the nitrogen-doped carbon shell, and the core-shell structured CoP@C cubes are obtained.

The morphology evolution during the preparation process was analyzed by scanning electron microscopy (SEM). The obtained CoCo-PBA precursors exhibit an angular cubic shape with a uniform size of approximately 800 nm (Figure 2a and d). During the phosphorization process, the CoCo-PBA precursors are converted into the porous CoP cubic with a slight reduction in size and increased surface roughness (Figure 2b and e). The

Encouragingly, the CoP@C still retains the cube morphology after the coating and carbonization of the PDA layer (Figure 2c,f, and S1). The obviously increased size and the smooth surface of CoP@C confirm the successful encapsulation of the carbon layer. The EDS elemental mapping images (Figure 2g) demonstrate that the Co, P, C, and N are uniformly distributed over the CoP@C structure.

The microstructure of CoP@C composite was examined by Transmission electron microscopy (TEM). As displayed in Figure 3a, the CoP cube is coated with a uniform carbon layer (~60 nm), forming a core-shell structure. The solitary CoP@C particle shows an average size of about 700 nm, consistent with SEM results. The high-resolution TEM (HRTEM, Figure 3b) image

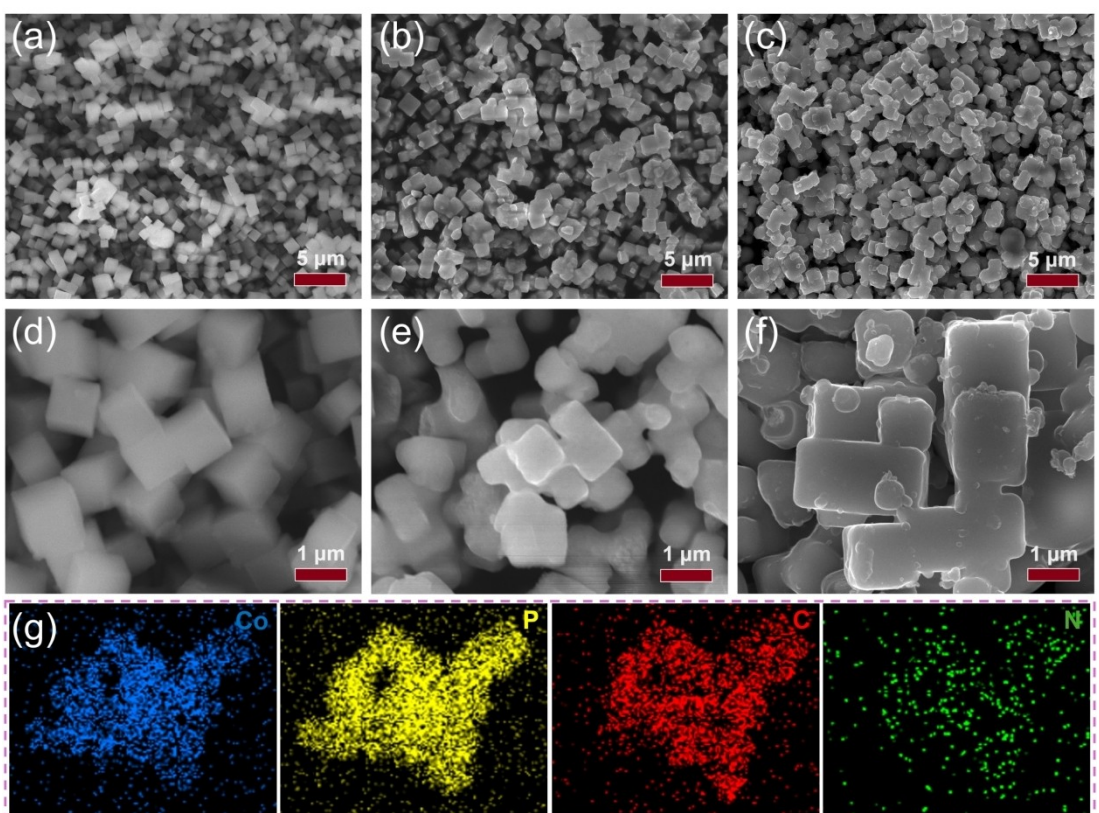


Figure 2. SEM images of (a, d) CoCo-PBA precursors, (b, e) CoP intermediates, and (c, f) CoP@C cubes; (g) EDS mapping images of CoP@C cubes with detected elements of Co, P, C, N.

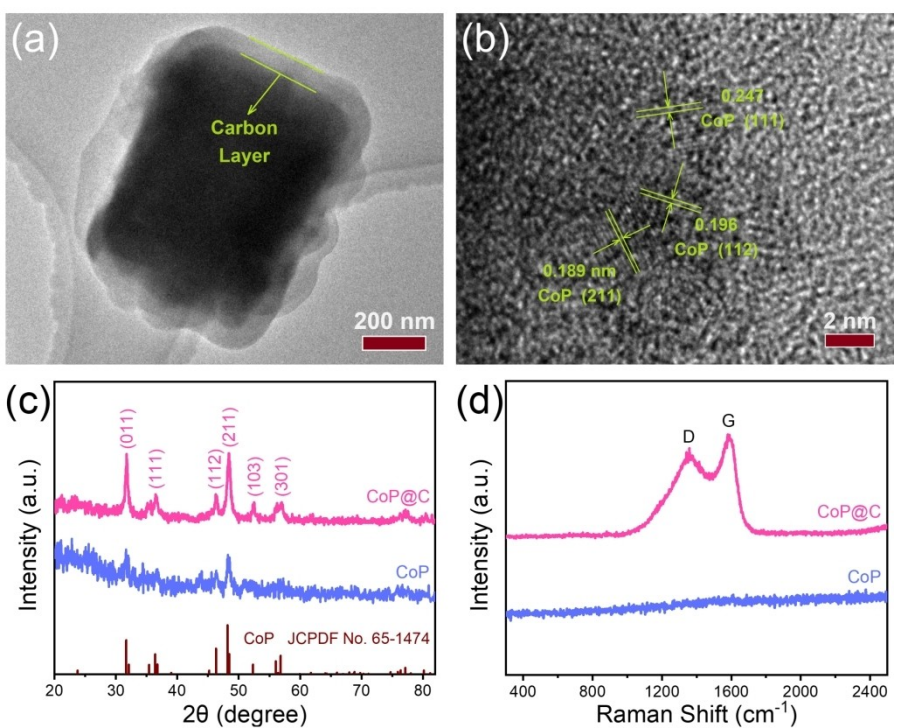


Figure 3. (a) TEM and (b) HRTEM images of CoP@C cubes; (c) XRD patterns and (d) Raman spectra of CoP@C and pure CoP.

of CoP@C reveals well-defined interplanar fringes with lattice distances of 0.247, 0.196, and 0.189 nm, which belong to the (111), (112), and (211) planes of CoP phase (JCPDS No.65-1474),^[14] respectively.

The phase transition of the synthesized samples was inspected using X-ray diffraction (XRD). As illustrated in Figure S2, the CoCo-PBA precursors exhibit distinct diffraction peaks at 17.4°, 24.7°, 35.2°, and 39.5°, corresponding to the cubic phase of $\text{Co}_3[\text{Co}(\text{CN})_6]_2$ with space group Fm-3 m.^[13] Following phosphating treatment, the diffraction peak of CoCo-PBA disappears while new peaks emerge at 31.7° and 48.3° (Figure 3c), which can be assigned to the (011) and (211) crystal faces of CoP,^[15] indicating a successful transformation from CoCo-PBA to CoP. Additionally, an increase in both the number and intensity of the diffraction peaks can be observed for the CoP@C composites after high-temperature annealing in Figure 3c, suggesting enhanced crystallinity. Notably, no diffraction peaks associated with the carbon layer are observed due to its amorphous nature, as also evident from the TEM image. Figure 3d displays the Raman spectra of CoP and CoP@C, in which two distinct signal peaks centered at 1360 and 1587 cm^{-1} are ascribed to disordered carbon (D-band) and graphitic carbon (G-band),^[16] respectively. The calculated I_G/I_D ratio is 1.18, indicating that the carbon layer has a high degree of graphitization and good electronic conductivity,^[17] which is beneficial for rapid sodium storage kinetics. The Fourier transform infrared (FT-IR) spectra of CoP and CoP@C are presented in Figure S3. The disappearance of the $\text{C}\equiv\text{N}$ tensile vibration peak representing CoCo-PBA at 2175 cm^{-1} and the emergence of the Co—P tensile vibration peak at 742 cm^{-1} further validate

the complete transformation of CoCo-PBA into CoP after phosphorization.^[14b,18]

The X-ray photoelectron spectroscopy (XPS) analysis was conducted to probe the chemical composition and bonding states of CoP@C composites. Figure S4 clearly confirms the presence of Co, P, C, and N elements, which is in line with the EDS mapping results mentioned earlier. In the high-resolution spectrum of Co 2p (Figure 4a), the two characteristic peaks at 797.6 and 781.5 eV are attributed to Co 2p_{1/2} and Co 2p_{3/2} of the Co species involved in the CoP phase.^[19] Furthermore, signal peaks at 802.7 and 785.6 eV correspond to oxidized forms of Co represented by Co 2p_{1/2} and Co 2p_{3/2} signals.^[20] Moving on to the P 2p spectra (Figure 4b), it is worth noting that the main peak at a binding energy of 133.7 eV can be ascribed to P—O bonding due to inevitable surface oxidation occurring in the case of CoP@C samples.^[21] The C 1s spectrum presented in Figure 4c can be deconvoluted into three distinct peaks: a major peak centered around 284.8 eV representing C—C bonding, and two additional peaks located at 286.0 and 287.1 eV corresponding to the C—N and O—C=O bonding, respectively.^[22] Figure 4d illustrates that the N 1 s spectrum is fitted by three peaks including pyridine-N, pyrrole-N, and graphite-N with binding energies of 400.6, 401.8, and 402.6 eV,^[23] respectively. The presence of pyridine-N and pyrrole-N enhances the availability of active sites for sodium ion reaction and storage, whereas graphite-N improves the electrical conductivity of the carbon matrix.^[24]

The sodium storage property of CoP@C was examined through cyclic voltammetry (CV) tests within a voltage range of 3–0.01 V at 0.1 mVs^{-1} (Figure 5a). During the initial cathodic

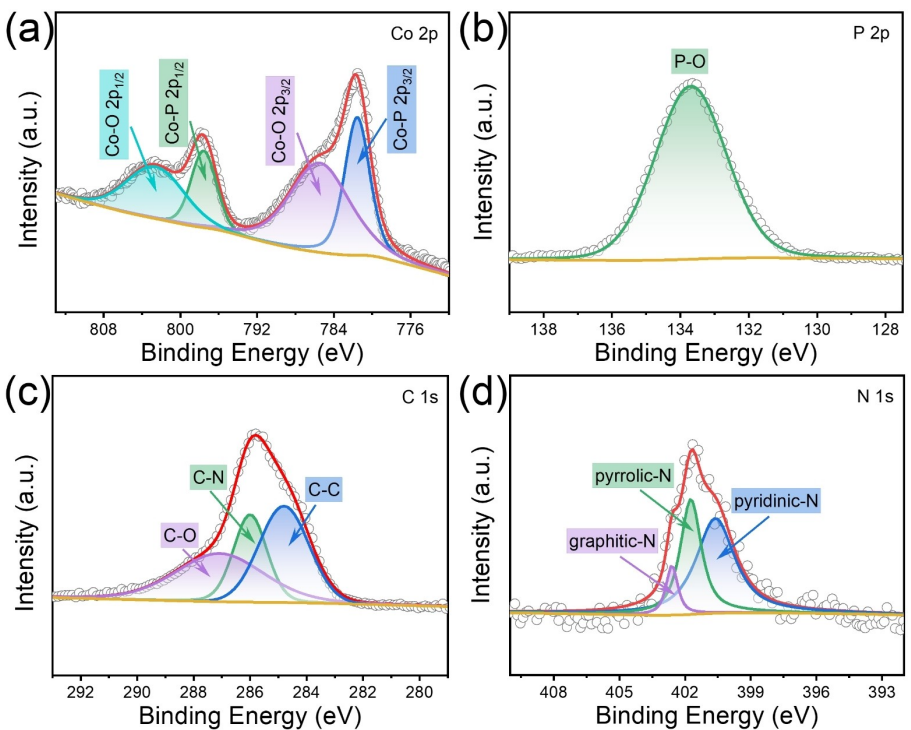


Figure 4. High-resolution XPS spectra of CoP@C composites: (a) Co 2p, (b) P 2p, (c) C 1s, and (d) N 1s regions.

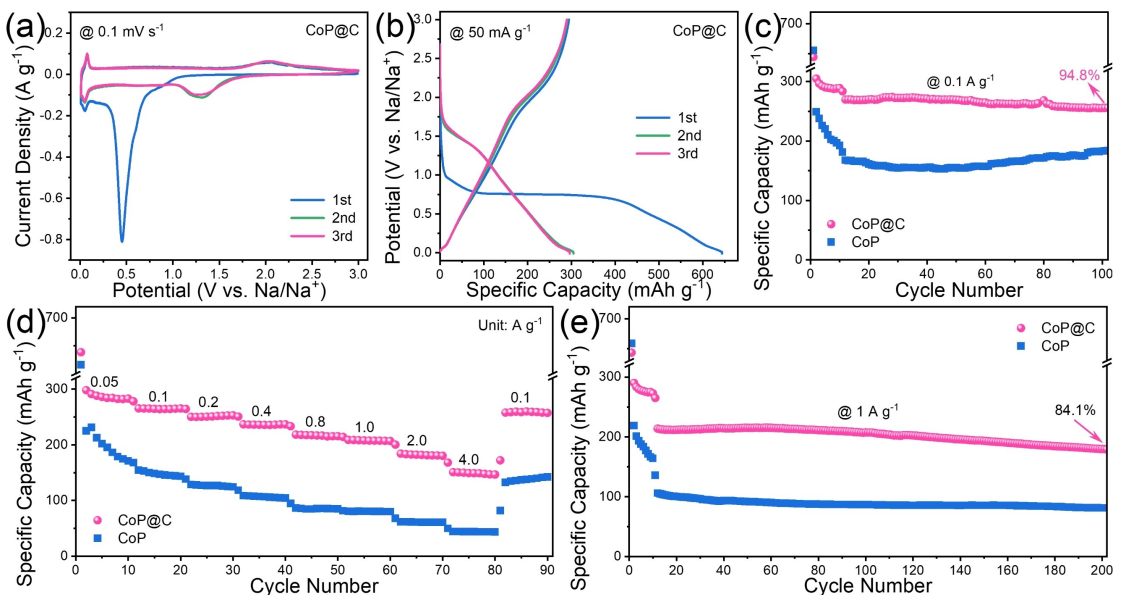


Figure 5. (a) CV curves at 0.1 mV s^{-1} and (b) galvanostatic charge/discharge profiles at 50 mA g^{-1} of the CoP@C electrode; (c) cyclic performance at 0.1 A g^{-1} , (d) rate capability from 0.05 to 4.0 A g^{-1} , and (e) cycle life at a high rate of 1.0 A g^{-1} of CoP@C and pure CoP electrodes.

scan, a reduction peak at 0.45 V is observed, indicating the conversion reaction between CoP and Na to form Na_3P and Co, as well as the formation of solid electrolyte interface (SEI) films.^[20] Upon the subsequent anodic scanning, the oxidation peak at 2.04 V corresponds to the reverse reaction of the above conversion reaction.^[9a] Additionally, a pair of redox peaks are identified at 0.05 V , which can be attributed to the insertion and removal of solvated Na^+ within the carbon component,

representing a unique phenomenon in ether-based electrolytes.^[25] As cycling progresses, the reduction peak shifts towards 1.30 V , attributing to significant structural changes occurring during the initial discharge.^[26] Moreover, the well-overlapped CV curves indicate the excellent electrochemical reversibility of the CoP@C electrode. In contrast, pure CoP exhibits much weaker redox peaks with increasing attenuation

amplitude among cycling (Figure S5a), suggesting inferior reaction kinetics and reversibility.

Figure 5b shows the charge/discharge profiles of CoP@C electrode at different cycles. The initial charge/discharge capacity of CoP@C is measured at $294.8/644.2 \text{ mAh g}^{-1}$, and the significant capacity loss is due to electrolyte decomposition and the formation of SEI film. Subsequent cycles exhibit well-preserved charge/discharge profiles with negligible capacity attenuation. However, for the pure CoP electrode (Figure S5b), discharge capacity rapidly declines from 249.2 to 192.5 mAh g^{-1} after ten cycles. The cycling stability of CoP@C and pure CoP electrodes are compared at 0.1 A g^{-1} (Figure 5c and S6). Apparently, the CoP@C electrode exhibits a superior reversible capacity compared to the pure CoP electrode throughout the entire cycling process, demonstrating a remarkable capacity retention rate of 94.8% after 100 cycles. The rate capabilities of CoP@C and pure CoP electrodes were evaluated at various current densities (Figure 5d). As the current density increases from 0.05 to 4.0 A g^{-1} , the reversible capacities of the CoP@C electrode exhibit values of $282.9, 265.2, 252.8, 236.7, 215.4, 206.8, 180.8$, and 146.7 mAh g^{-1} , respectively. When reverting back to 0.1 A g^{-1} , the capacity can be promptly restored without any significant delay or degradation in performance, demonstrating its exceptional structural tolerance. Conversely, for the pure CoP electrode under increasing current density conditions up to a maximum of 4.0 A g^{-1} , it experiences rapid capacity decay with only a release of 43.6 mAh g^{-1} . The capacity-voltage curves for both electrodes at each current density are presented in Figure S7. It can be observed that the charge/discharge profiles for the CoP@C electrode are less affected by changes in current and exhibit reduced polarization. Notably, the CoP@C electrode prepared in this work exhibits superior capacity retention at high-rate conditions compared to other cobalt

phosphide composite electrodes documented in the literature (Figure S8).

In addition, the cycle life of CoP@C and pure CoP electrodes was compared at a high rate of 1.0 A g^{-1} . Even after undergoing 200 cycles, the CoP@C electrode maintains an impressive reversible capacity of 180.0 mAh g^{-1} , surpassing that of pure CoP by an additional 100 mAh g^{-1} (Figure 5e). To assess the structural stability of the CoP@C electrode, the disassembly of the cycled battery was conducted to examine morphological changes in the electrode. As depicted in Figure S9, following repeated charge/discharge cycles, the overall structure of the CoP@C electrode remains unaltered with no indications of fracturing. Furthermore, individual CoP@C particles maintain their cubic morphology without experiencing breakage or aggregation, confirming the exceptional structural robustness of the CoP@C electrode.

To analyze the kinetic behaviors of both CoP@C and pure CoP electrodes, CV tests at scan rates ranging from 0.1 to 1.0 mV s^{-1} were conducted. As shown in Figure 6a, the CV curves of the CoP@C electrode display a consistent shape with increasing sweep speeds, albeit with oxidation peaks shifting towards higher potentials and reduction peaks shifting towards lower potentials. On the contrary, significant changes in CV curves are observed for the pure CoP electrode, including a new oxidation peak at 0.5 V , indicating poor reversibility (Figure S10a). By examining the power law relationship between peak current (i) and scanning rate (v): $i = av^b$, it is possible to qualitatively determine whether diffusion control or capacitance dominates in electrochemical processes. Herein, a represents a constant and b denotes a variable exponent.^[27] Generally, when the b -value approaches 0.5 , diffusion control prevails, whereas an approach towards 1.0 indicates capacitance dominance. In the current work, the b -values of both electrodes are within the range of 0.5 – 1.0 (Figure 6b and S10b), suggesting that the

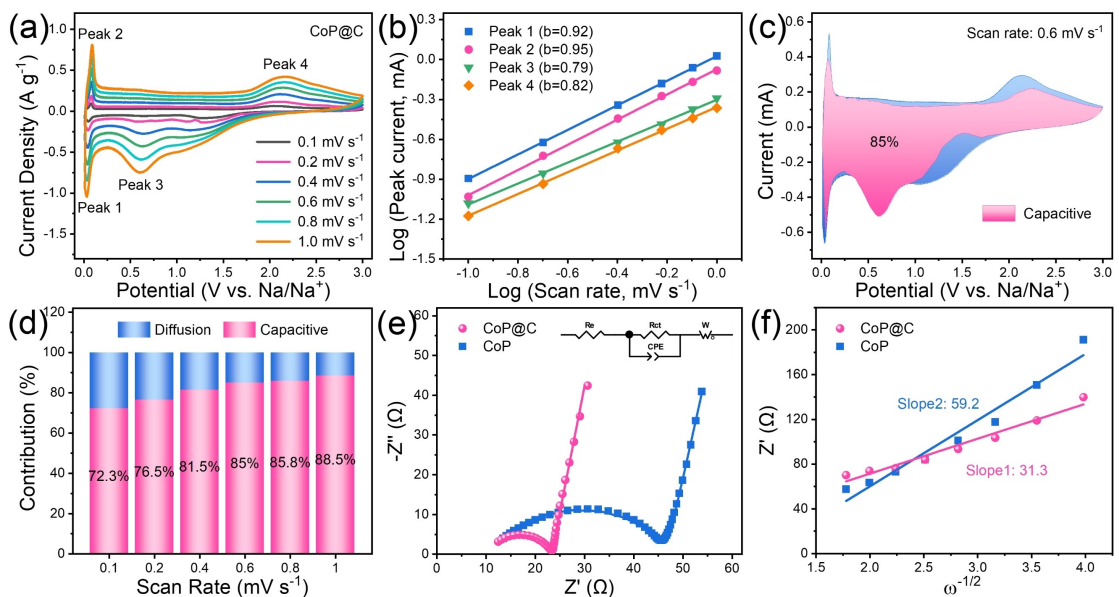


Figure 6. Kinetics behavior analysis of the CoP@C electrode: (a) CV curves at different scan rates; (b) calculation of b -values based on the linear fitting results of $\log(v)$ vs. $\log(i)$; (c) capacitive contribution ratio at 0.6 mV s^{-1} ; (d) diffusion (blue part) and capacitive (pink part) contribution ratios from 0.1 to 1.0 mV s^{-1} ; (e) Nyquist plots compared to the pure CoP electrode; (f) linear fitting relationship between $\omega^{-1/2}$ and Z' .

capacitance and diffusion processes are involved in their respective electrochemical mechanisms. Furthermore, the specific capacitive (k_1v) and diffusion control ratios ($k_2v^{1/2}$) can be quantitatively determined using the following formula: $i(V) = k_1v + k_2v^{1/2}$.^[28] The capacitive contribution of the CoP@C electrode at a scan rate of 0.6 mVs^{-1} is depicted in Figure 6c. The pink region representing capacitive contribution accounts for 85% of the entire CV profile, which is significantly higher than that of the pure CoP electrode (40.7%, Figure S10c). Similarly, the capacitive contribution ratios were calculated at different scan rates (Figure 6d and S10d). The capacitance contribution ratio of the CoP@C electrode continuously increases with the increment in sweep speeds, ultimately reaching 88.5%, demonstrating superior sodium storage kinetics in comparison with the pure CoP electrode (49.2%).

The charge transfer kinetics of CoP@C and pure CoP electrodes was further explored by electrochemical impedance spectroscopy (EIS). As depicted in Figure 6e, both plots display a semicircle in the high-frequency region and a diagonal line in the low-frequency region, which represent the charge transfer resistance (R_{ct}) and the Warburg diffusion process, respectively.^[29] Notably, the CoP@C electrode demonstrates a significantly lower R_{ct} value (12.6Ω) compared to that of the pure CoP electrode (35.0Ω), indicating that the carbon layer coating greatly enhances electrode conductivity. To gain deeper insights into the advantages of the CoP@C core-shell structure for storing sodium ions, the Na^+ diffusion coefficient (D_{Na^+}) is calculated using the following equation: $D_{\text{Na}^+} = R^2 T^2 / 2A^2 n^4 F^4 C^2 \sigma^2$.^[30] Here, R , A , T , F , C , n , and σ represent the gas constant, electrode area, Kelvin temperature, Faraday constant, Na^+ concentration, charge transfer number, and Warburg coefficient, respectively. The slopes of Z' vs. $\omega^{-1/2}$ in the Warburg region for both CoP@C and pure CoP electrodes are depicted in Figure 6f, with σ -values determined as 31.3 and 59.2. This clearly indicates that the CoP@C electrode exhibits a higher D_{Na^+} value, further validating its fast sodium ion transport dynamics. Furthermore, the EIS analysis was conducted on the cycled battery. As illustrated in Figure S11, the R_{ct} value of the CoP@C electrode decreased to 5.2Ω after cycling, which further highlights the excellent interface stability of the CoP@C electrode during prolonged cycling.

According to the analysis above, the outstanding sodium storage performance of CoP@C cubes could be attributed to the superior core-shell structure. Firstly, the surface-coated carbon coating could act as an elastic buffering layer to accommodate volume changes of CoP and prevent particle agglomeration/crushing during long charge/discharge cycling, thereby enhancing electrode cycle stability. Secondly, the nitrogen-doped carbon coating significantly improves the electronic conductivity of composites for rapid electron transportation. Lastly, the unique core-shell structure of CoP@C promotes fast interfacial ion transport kinetics, contributing to high-rate sodium storage performance through enhanced surface capacitance behavior.

3. Conclusions

In summary, the CoP@C cube composites with core-shell structure were successfully fabricated through *in situ* phosphating and carbon coating on CoCo-PBA. The surface of CoP particles is coated by a uniform nitrogen-rich carbon nanolayer, significantly improving the electronic conductivity of composites. Moreover, the unique core-shell structure not only alleviates volume expansion during the sodiation process but also provides high-speed pathways for rapid electron/ion transport. Consequently, the CoP@C electrode demonstrates remarkable cycling stability and excellent rate performance, exhibiting a capacity retention rate of 94.8% after 100 cycles at 0.1 Ag^{-1} and delivering a high reversible capacity of 146.7 mAhg^{-1} at a high rate of 4.0 Ag^{-1} .

Acknowledgements

This work was financially supported by the Natural Science Foundation of Qinghai Province (2024-ZJ-930), the National Natural Science Foundation of China (52272239), and the Key Research and Technological Achievements Transformation Plan Project of Inner Mongolia Autonomous Region (2023YFHH0063).

Conflict of Interests

The authors declare no conflict of interest.

Data Availability Statement

Data will be made available on request.

Keywords: cobalt phosphide • carbon • core-shell structure • anodes • sodium-ion batteries

- [1] a) Q. Liu, Z. H. E. Hu, W. Li, C. Zou, H. Jin, S. Wang, S. Chou, S. X. Dou, *Energy Environ. Sci.* **2021**, *14*, 158–179; b) X. Zhang, Z. Hou, M. Jiang, J. Peng, H. Ma, Y. Gao, J.-G. Wang, *Small* **2024**, *20*, 2311778; c) C. Yang, S. Xin, L. Mai, Y. You, *Adv. Energy Mater.* **2020**, *11*, 2000974; d) Y. Tian, G. Zeng, A. Rutt, T. Shi, H. Kim, J. Wang, J. Koettgen, Y. Sun, B. Ouyang, T. Chen, Z. Lun, Z. Rong, K. Persson, G. Ceder, *Chem. Rev.* **2020**, *121*, 1623–1669; e) Y. Cao, X. Cao, X. Dong, X. Zhang, J. Xu, N. Wang, Y. Yang, C. Wang, Y. Liu, Y. Xia, *Adv. Funct. Mater.* **2021**, *31*, 2102856; f) Y. Cao, C. Yang, Y. Liu, X. Xia, D. Zhao, Y. Cao, H. Yang, J. Zhang, J. Lu, Y. Xia, *ACS Energy Lett.* **2020**, *5*, 3788–3796
- [2] P. K. Nayak, L. Yang, W. Brehm, P. Adelhelm, *Angew. Chem. Int. Ed.* **2018**, *57*, 102–120.
- [3] J. Y. Hwang, S. T. Myung, Y. K. Sun, *Chem. Soc. Rev.* **2017**, *46*, 3529–3614.
- [4] a) W. Zhang, F. Zhang, F. Ming, H. N. Alshareef, *EnergyChem* **2019**, *1*, 100012; b) Y. Li, M. Chen, B. Liu, Y. Zhang, X. Liang, X. Xia, *Adv. Energy Mater.* **2020**, *10*, 2000927; c) W. Zhang, J. Lu, Z. Guo, *Mater. Today* **2021**, *50*, 400–417
- [5] a) Q. Li, D. Yang, H. Chen, X. Lv, Y. Jiang, Y. Feng, X. Rui, Y. Yu, *SusMat* **2021**, *1*, 359–392; b) F. Chen, J. Xu, S. Wang, Y. Lv, Y. Li, X. Chen, A. Xia, Y. Li, J. Wu, L. Ma, *Adv. Sci.* **2022**, *9*, 2200740; c) L. Wang, Q. Li, Z. Chen, Y. Wang, Y. Li, J. Chai, N. Han, B. Tang, Y. Rui, L. Jiang, *Small* **2024**, *20*, 2310426

- [6] a) W. Liu, H. Zhi, X. Yu, *Energy Storage Mater.* **2019**, *16*, 290–322; b) G. Chang, Y. Zhao, L. Dong, D. P. Wilkinson, L. Zhang, Q. Shao, W. Yan, X. Sun, J. Zhang, *J. Mater. Chem. A* **2020**, *8*, 4996–5048
- [7] W. Zhang, T. Liu, Y. Wang, Y. Liu, J. Nai, L. Zhang, O. Sheng, X. Tao, *Nano Energy* **2021**, *90*, 106475.
- [8] a) Y. Liu, J. Wang, Q. Shi, M. Yan, S. Zhao, W. Feng, R. Qi, J. Xu, J. Luo, J. Zhang, Y. Zhao, *Angew. Chem. Int. Ed.* **2023**, *62*, e202303875; b) L. Ren, X. Zhou, Z. Hou, Z. Luo, Y. Huyan, C. Wei, J.-G. Wang, *J. Colloid Interface Sci.* **2024**, *664*, 511–519; c) T. Zeng, H. He, H. Guan, R. Yuan, X. Liu, C. Zhang, *Angew. Chem. Int. Ed.* **2021**, *60*, 12103–12108
- [9] a) Q. Li, Q. Jiao, H. Li, Y. Yan, C. Lu, X. Shen, T. Gu, W. Zhou, Y. Zhao, H. Li, C. Feng, *J. Mater. Chem. A* **2022**, *10*, 21690–21700; b) S. Park, D. Kim, M. Jang, T. Hwang, S. J. Hwang, Y. Piao, *Nanoscale* **2022**, *14*, 6184–6194; c) Y. Zhang, G. Wang, L. Wang, L. Tang, M. Zhu, C. Wu, S. X. Dou, M. Wu, *Nano Lett.* **2019**, *19*, 2575–2582
- [10] a) X. Song, S. Song, D. Wang, H. Zhang, *Small Methods* **2021**, *5*, 2001000; b) X. Jiang, Q. Xie, G. Lu, Y. Wang, T. Liu, Y. Liu, X. Tao, J. Nai, *Small Methods* **2022**, *6*, 2200377; c) Y. Wang, R. Chen, E. H. Ang, Y. Yan, Y. Ding, L. Ke, Y. Luo, K. Rui, H. Lin, J. Zhu, *Adv. Sustainable Syst.* **2021**, *5*, 2100223
- [11] a) Y. Von Lim, S. Huang, Y. Zhang, D. Kong, Y. Wang, L. Guo, J. Zhang, Y. Shi, T. P. Chen, L. K. Ang, H. Y. Yang, *Energy Storage Materials* **2018**, *15*, 98–107; b) Z. Li, L. Zhang, X. Ge, C. Li, S. Dong, C. Wang, L. Yin, *Nano Energy* **2017**, *32*, 494–502
- [12] a) Q. Wang, B. Wang, Z. Zhang, Y. Zhang, J. Peng, Y. Zhang, H. Wu, *Inorg. Chem. Front.* **2018**, *5*, 2605–2614; b) L. Ren, M. Jiang, Z. Hou, N. Li, D. Nan, J.-G. Wang, *Appl. Surf. Sci.* **2023**, *612*, 155952
- [13] Y. Feng, X. Y. Yu, U. Paik, *Chem. Commun.* **2016**, *52*, 6269–6272.
- [14] a) Q. Liu, Z. Hu, Y. Liang, L. Li, C. Zou, H. Jin, S. Wang, H. Lu, Q. Gu, S. L. Chou, Y. Liu, S. X. Dou, *Angew. Chem. Int. Ed.* **2020**, *59*, 5159–5164; b) H. Ma, M. Jiang, Z. Hou, T. Li, X. Zhang, Y. Gao, J. Peng, Y. Li, J.-G. Wang, *Energy Storage Mater.* **2024**, *70*, 103411; c) L. Han, M. Zhang, H. Wang, P. Li, W. Wei, J. Shi, M. Huang, Z. Shi, W. Liu, S. Chen, *Nanoscale* **2020**, *12*, 24477–24487
- [15] X. Ge, Z. Li, L. Yin, *Nano Energy* **2017**, *32*, 117–124.
- [16] Y. Wang, Y. V. Lim, S. Huang, M. Ding, D. Kong, Y. Pei, T. Xu, Y. Shi, X. Li, H. Y. Yang, *Nanoscale* **2020**, *12*, 4341–4351.
- [17] W. Huang, H. Shangguan, X. Zheng, C. Engelbrekt, Y. Yang, S. Li, K. Mølhave, X. Xiao, X. Lin, L. Ci, P. Si, *Electrochim. Acta* **2021**, *395*, 139112.
- [18] P. Ge, S. Li, H. Shuai, W. Xu, Y. Tian, L. Yang, G. Zou, H. Hou, X. Ji, *Adv. Mater.* **2018**, *31*, 1806092.
- [19] B. Wang, K. Chen, G. Wang, X. Liu, H. Wang, J. Bai, *Nanoscale* **2019**, *11*, 968–985.
- [20] D. Zhao, R. Zhao, S. Dong, X. Miao, Z. Zhang, C. Wang, L. Yin, *Energy Environ. Sci.* **2019**, *12*, 2422–2432.
- [21] H. Su, Y. Zhang, X. Liu, F. Fu, J. Ma, K. Li, W. Zhang, J. Zhang, D. Li, J. *Colloid Interface Sci.* **2021**, *582*, 969–976.
- [22] S. Tao, J. Xu, T. Xie, S. Chu, D. Wu, B. Qian, S. Chen, L. Song, *J. Power Sources* **2021**, *500*, 229975.
- [23] C. Ma, Y. Hou, K. Jiang, L. Zhao, T. Olsen, Y. Fan, J. Jiang, Z. Xu, Z. Ma, D. Legut, H. Xiong, X.-Z. Yuan, *Chem. Eng. J.* **2021**, *413*, 127449.
- [24] X. Hua, X. Sun, S. J. Yoo, B. Evanko, F. Fan, S. Cai, C. Zheng, W. Hu, G. D. Stucky, *Nano Energy* **2019**, *56*, 828–839.
- [25] C. Wang, J. Yan, T. Li, Z. Lv, X. Hou, Y. Tang, H. Zhang, Q. Zheng, X. Li, *Angew. Chem. Int. Ed.* **2021**, *60*, 25013–25019.
- [26] H. M. Saleem, M. Jamil, M. Tabish, A. H. Khoja, A. Li, D. Wang, H. Song, *ACS Appl. Energy Mater.* **2023**, *6*, 9885–9896.
- [27] G. Sun, H. Lin, R. Tian, Z. Wei, X. Wang, X. Jin, S. Yao, G. Chen, Z. Shen, F. Du, *Nano Res.* **2023**, *16*, 9407–9415.
- [28] T. Wang, D. Legut, Y. Fan, J. Qin, X. Li, Q. Zhang, *Nano Lett.* **2020**, *20*, 6199–6205.
- [29] a) Z. Li, H. Zhao, Z. Du, L. Zhao, J. Wang, Z. Zhang, *J. Power Sources* **2020**, *465*, 228253; b) B. Xu, Y. Cao, J. Xu, D. Zhao, N. Wang, B. Wang, *Batteries & Supercaps* **2023**, *6*, e202300241
- [30] H. Li, Y. He, Q. Wang, S. Gu, L. Wang, J. Yu, G. Zhou, L. Xu, *Adv. Energy Mater.* **2023**, *13*, 2302901.

Manuscript received: July 9, 2024

Revised manuscript received: August 18, 2024

Accepted manuscript online: August 28, 2024

Version of record online: October 23, 2024